Article | Open Access

Energy Materials

Gao et al. Energy Mater. 2026, 6, 600100 DOI:10.20517/energymater.2026.168

Enhanced oxygen evolution of FeNiMoRuZn sulfide through Zn-enabled multiscale stabilization

Shasha Gao[1,2], Jinteng Guan[1], Hongmei Chen[1], Feifei Mao[1,3], Jiacong Lei[2], Dong Guo[2,*], Yang Gao[4,*], Yingbin Li[1,*], Gonglei Shao[2,*]

Keywords:
High-entropy sulfide, electrocatalyst, Zn-enabled multiscale stabilization, oxide pathway mechanism, oxygen evolution reaction

Citation: Gao, S.; Guan, J.; Chen, H.; Mao, F.; Lei, J.; Guo, D.; Gao, Y.; Li, Y.; Shao, G. Enhanced oxygen evolution of FeNiMoRuZn sulfide through Zn-enabled multiscale stabilization. *Energy Mater.* **2026**, *6*, 600100. https://dx.doi.org/10.20517/energymater.2026.168

Received: 11 Jun 2026
First Decision: 1 Jul 2026
Revised: 12 Jul 2026
Accepted: 5 Aug 2026
Published: 14 Aug 2026

Academic Editor:
Yuhui Chen
Copy Editor:
Ping Zhang
Production Editor:
Ping Zhang

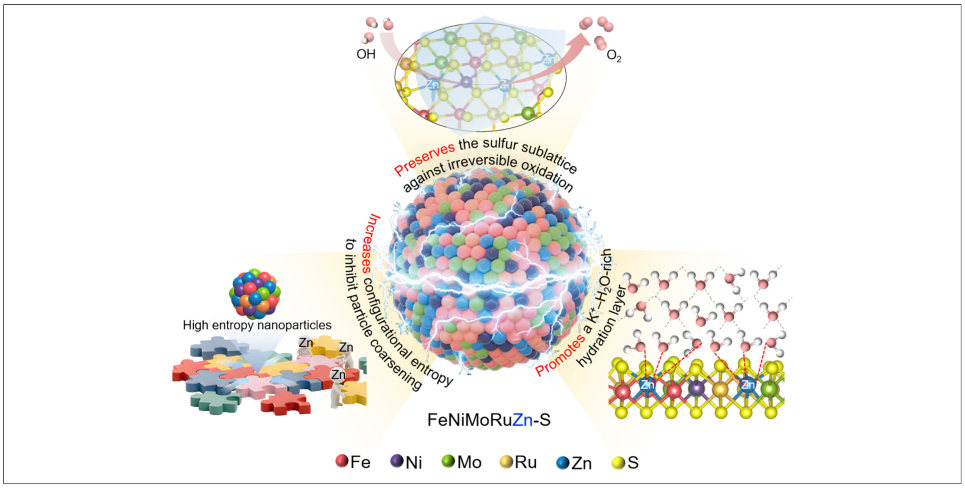

Abstract

Transition metal sulfides are promising oxygen evolution reaction (OER) electrocatalysts; however, they suffer from structural degradation under anodic conditions. Herein, we report that the incorporation of Zn into a quaternary FeNiMoRu-S system enables the formation of a five-metal, high-entropy sulfide (FeNiMoRuZn-S) with a dramatically enhanced OER performance, achieved through Zn-enabled multiscale stabilization. Specifically, Zn delivers three distinct yet interrelated stabilizing effects. At the nanoscale, it increases configurational entropy to inhibit particle coarsening and generate uniformly dispersed nanoparticles. At the interface, it promotes the enrichment of K^+-H_2O hydration layers to boost interfacial water activation. At the atomic scale, it stabilizes the sulfur sublattice against irreversible oxidation, thereby maintaining structural integrity under long-term cycling. Density functional theory calculations further reveal that Zn induces

[1]Key Laboratory of Microelectronics and Energy of Henan Province, Department of Physics and Electronic Engineering, Xinyang Normal University, Xinyang 464000, Henan, China.
[2]Interdisciplinary Research Center for Sustainable Energy Science and Engineering (IRC4SE^2), School of Chemical Engineering, Zhengzhou University, Zhengzhou 450001, Henan, China.
[3]Department of System Semiconductor Engineering, Cheongju University, Cheongju 28503, South Korea.
[4]Collaborative Innovation Center, Henan Academy of Sciences, Zhengzhou 450046, Henan, China.

*Correspondence to: Prof. Gonglei Shao, Dr. Dong Guo, Interdisciplinary Research Center for Sustainable Energy Science and Engineering (IRC4SE^2), School of Chemical Engineering, Zhengzhou University, Zhengzhou 450001, Henan, China. E-mail: shaogonglei@zzu.edu.cn; guodong@gs.zzu.edu.cn; Prof. Yingbin Li, Key Laboratory of Microelectronics and Energy of Henan Province, Department of Physics and Electronic Engineering, Xinyang Normal University, Xinyang 464000, Henan, China. E-mail: liyingbin@xynu.edu.cn; Dr. Yang Gao, Collaborative Innovation Center, Henan Academy of Sciences, Zhengzhou 450046, Henan, China. E-mail: yanggao@hnas.ac.cn

synergistic electronic modulation of dual active sites, optimizing electron transfer and intermediate adsorption during the oxide pathway mechanism. The resulting catalyst demonstrates a low overpotential of 207 mV at 10 mA cm^{-2}, a Tafel slope of 47.6 mV dec^{-1}, and stable performance during a cumulative 200 h stepwise stability test at current densities of 10, 50, 100 and 250 mA cm^{-2}. Notably, in an anion exchange membrane water electrolyzer, Pt/C||FeNiMoRuZn-S delivers stable performance at an industrial-level current density of 500 mA cm^{-2} for 200 h, significantly outperforming its Zn-free counterpart. This work demonstrates that rational elemental selection in high-entropy systems can orchestrate stability across multiple length scales to realize high activity and durability in sulfide-based OER electrocatalysts.

INTRODUCTION

The large-scale deployment of water electrolysis for green hydrogen production critically depends on the development of efficient, durable, and earth-abundant electrocatalysts for the oxygen evolution reaction (OER)[1-3]. Despite their high activity, state-of-the-art IrO_2- and RuO_2-based catalysts suffer from scarcity and high cost, necessitating the exploration of nonprecious alternatives[4-6]. Among them, transition metal sulfides (TMSs) have attracted considerable attention due to their metallic conductivity, tunable electronic structures, and rich redox chemistry, which collectively enable competitive OER performance in alkaline media[7-9]. However, the practical application of TMSs is severely impeded by their intrinsic instability at anodic potentials. During OER operation, the sulfur anion sublattice is thermodynamically prone to irreversible oxidation to sulfate species, leading to structural disintegration, surface passivation, and rapid performance decay[10,11]. This degradation pathway represents a fundamental bottleneck that cannot be fully addressed by conventional strategies such as nanostructuring, heteroatom doping, or hybridization with conductive matrices. These approaches often enhance initial activity but fail to preserve the integrity of the sulfur framework over extended cycling[12-15].

To address this challenge, high-entropy materials (HEMs), which incorporate five or more principal elements in near-equimolar ratios, have recently been extended to include sulfide systems[16-18]. These high-entropy sulfides (HESs) leverage high configurational entropy and sluggish diffusion effects to stabilize single-phase nanostructures, and several reports have demonstrated impressive OER activities[19-22]. Nevertheless, a critical gap remains as most studies focus on activity metrics without providing direct evidence of sulfur stability under operational conditions. Moreover, even in state-of-the-art HESs, post-OER characterization often reveals partial surface oxidation or sulfate formation, indicating that high entropy alone is insufficient to prevent anion corrosion[23-26]. This limitation underscores the need for a rational design strategy that explicitly targets sulfur sublattice stabilization, and Zn has emerged as a compelling candidate for this purpose. Due to the electrochemically inert nature within typical OER potential windows [1.2-1.7 V *vs.* reversible hydrogen electrode (RHE)], Zn exhibits high sulfide formation enthalpies ($\Delta H_f \approx$ -206 kJ mol^{-1} for ZnS) and strong Zn-S covalent bonding, which can effectively anchor sulfur atoms and suppress oxidative dissolution[27,28]. Recent studies on phosphides and selenides have further confirmed that Zn incorporation enhances structural coherence and mitigates anion loss during harsh electrochemical processes[29-31].

Herein, we demonstrate the rational design of a quinary high-entropy sulfide, FeNiMoRuZn-S (denoted M4Zn-S), in which Zn is intentionally introduced not as a passive constituent but as an active multiscale stabilizer. For comparison, the quaternary analog without Zn, FeNiMoRu-S (denoted M4-S), is also synthesized under identical conditions. The incorporation of Zn enables three interconnected stabilization effects: (i) at the nanoscale, it elevates configurational entropy to yield well-dispersed nanoparticles; (ii) at the interface, it promotes a K^+-H_2O-rich hydration layer that facilitates water activation; (iii) at the atomic scale, it preserves the sulfur sublattice against irreversible oxidation, thereby enabling reversible redox cycling of all

active metal centers. The resulting catalyst achieves a low overpotential of 207 mV at 10 mA cm^{-2} and maintains stable operation for 200 h. Notably, when integrated as the anode in an anion exchange membrane water electrolyzer (AEMWE) device, it delivers stable performance at an industrial-level current density of 500 mA cm^{-2} for 200 h, significantly outperforming its Zn-free counterpart. Density functional theory (DFT) analysis reveals that high-entropy engineering modulates the d-band centers of the Fe and Ni sites to optimize intermediate adsorption for favorable OER kinetics. The optimized d-band centers facilitate direct O-O coupling via the oxide pathway mechanism (OPM), markedly reduce the Gibbs free-energy change of the potential-determining step (PDS), and alleviate the structural degradation originating from lattice oxygen participation in the lattice oxygen-mediated mechanism (LOM), enabling M4Zn-S to simultaneously achieve an outstanding OER activity and durability. This work demonstrates that element-specific engineering beyond mere entropy maximization is essential for realizing durable sulfide-based OER electrocatalysts.

EXPERIMENTAL

Materials and reagents

$FeCl_2·4H_2O$ (98%), $NiCl_2$ (99%), $RuCl_3$ (99.5%), $MoCl_5$ (99.9%), $ZnCl_2$ (99%), Na_2S (99.5%), dodecylammonium chloride (99%) and anhydrous ethanol were purchased from the Alfa Reagent Company, and used in experiments without further purification.

Synthesis of M4Zn-S and M4-S catalyst

First, 0.1 mmol $FeCl_2·4H_2O$, 0.1 mmol $NiCl_2$, 0.1 mmol $RuCl_3$, 0.1 mmol $MoCl_5$, and 0.1 mmol $ZnCl_2$ were added into the reactor inner tank, followed by the addition of 2 mmol Na_2S, 0.5 mmol dodecylammonium chloride and 40 mL deionized water. Then, ultrasound was carried out for 10 min to form a uniform mixed solution, which was then put into the reaction kettle. The reaction kettle was put into the oil bath agitator and reacted at 150 °C for 6 h. After the reaction, the product was poured into a 50 mL centrifuge tube for centrifugation, then centrifuged with water and ethanol respectively, and then freeze-dried. The dried M4Zn-S sample was vacuumed for preservation. Similarly, the preparation of M4-S is the same as that of M4Zn-S, and the only difference is that no $ZnCl_2$ is added.

Electrochemical measurements

Linear sweep voltammetry tests were carried out via a CHI 760E electrochemical workstation, adopting a classic three-electrode testing system. The electrolyte was 1 M KOH, whose pH value was calibrated to 13.98. A Hg/HgO electrode served as the reference electrode, while a graphite rod acted as the counter electrode throughout all tests. To prepare uniform catalytic slurry, 2 mg of as-prepared catalysts were blended with 40 μL 5 wt% Nafion and 960 μL ethanol solvent. The mixed suspension was subjected to 60 min of continuous ultrasonication to achieve even dispersion. Two different working electrodes were fabricated in this work. For glassy carbon electrodes with a diameter of 3 mm, 20 μL of the homogenized catalyst suspension was drop-cast onto the electrode surface. Alternatively, 500 μL catalytic ink was deposited onto hydrophilic carbon paper substrates to reach a mass loading of 1 mg cm^{-2}. Prior to collecting all electrochemical data, high-purity nitrogen gas was purged through the alkaline electrolyte for roughly 30 min to saturate the solution. Every electrochemical curve was processed with iR compensation. Cyclic voltammetry tests were implemented under ambient temperature within the identical three-electrode assembly, with scanning rates at 5, 10, 20, 40, 60, 80, 120 and 160 mV s^{-1}. Electrochemical impedance spectroscopy was performed to acquire Nyquist curves of the catalysts, with the testing frequency ranging from 0.1 Hz up to 100 kHz. Long-term electrocatalytic durability of M4Zn-S was assessed via chronopotentiometry measurements under current densities of 10, 50, 100 and 250 mA cm^{-2}. The Tafel slope was extracted based on the formula $\eta = a + b\log(i)$[32], η stands for reaction overpotential, b represents the Tafel slope value, i corresponds to applied current density, and a refers to an undetermined constant term.

Theoretical

All first-principles computational simulations relying on DFT were completed within the Vienna Ab Initio Simulation Package (VASP). Generalized Gradient Approximation (GGA) combined with Perdew-Burke-Ernzerhof (PBE) functional was adopted to quantify exchange-correlation energy. Projector Augmented Wave (PAW) method was selected to depict interactions between electrons and ions. The cutoff energy for plane-wave basis sets was fixed at 400 eV. The convergence thresholds for electronic self-consistent iteration and atomic geometric relaxation were individually defined as 1×10^{-5} eV and 0.02 eV.

For all constructed surface slab models, a vacuum spacing exceeding 15 Å was inserted along the z-axis, eliminating spurious interlayer coupling induced by periodic boundary conditions. A 2 × 2 × 1 Monkhorst-Pack k-point grid was utilized to integrate electronic states across the Brillouin zone. Spin polarization effects were activated throughout all computational tasks to precisely reproduce intrinsic magnetic behaviors of target materials.

Adsorption energy values (E_{ads}) were quantified via:

$$E_{ads} = E_{total} - E_{surface} - E_{molecule} \quad (1)$$

In this formula, E_{total} corresponds to the overall energy of slab substrates with adsorbed intermediates, $E_{surface}$ stands for total energy of bare catalyst surfaces, and $E_{molecule}$ refers to the energy of independent gaseous reactant molecules[33].

The binding energies of three key intermediates (*OH, *O and *OOH) were calculated using:

$$\Delta E_{ads} = E_{species+cat.} - E_{cat.} - E_{species} \quad (2)$$

where $E_{species+cat.}$ and E_{cat}. separately represent total energies of catalysts with adsorbed fragments and clean catalyst substrates, while $E_{species}$ is the energy of the isolated species (OOH, O, OH), referenced to gas-phase H_2 and H_2O via the RHE model proposed by Nørskov *et al.*[33].

Corrected Gibbs free energy variations during adsorption processes were determined by:

$$\Delta G = \Delta E_{ad} + \Delta ZPE - T\Delta S \quad (3)$$

ΔZPE is the correction term accounting for zero-point vibrational energy, T represents room temperature fixed at 298.15 K, and ΔS refers to entropy change. Among all four core reaction steps of OER, the elementary step bearing the maximum Gibbs free energy gap (ΔG_1, ΔG_2, ΔG_3, ΔG_4) is identified as the reaction PDS. Theoretical overpotential values were derived purely from thermodynamic free energy differences rather than kinetic energy barriers. This simplification originates from the linear Brønsted-Evans-Polanyi (BEP) scaling relation linking reaction energies and activation barriers in heterogeneous catalysis, which was first proposed by Bligaard *et al.*[34].

RESULTS AND DISCUSSION

The rational design of multicomponent electrocatalysts has been substantially advanced by the high-entropy concept, wherein five or more principal elements in near-equimolar ratios stabilize single-phase crystal structures through high configurational entropy. Herein, we report the synthesis of a five-metal sulfide, M4Zn-S, via a hydrothermal route [Figure 1A]. By contrast, the quaternary analog M4-S is synthesized using

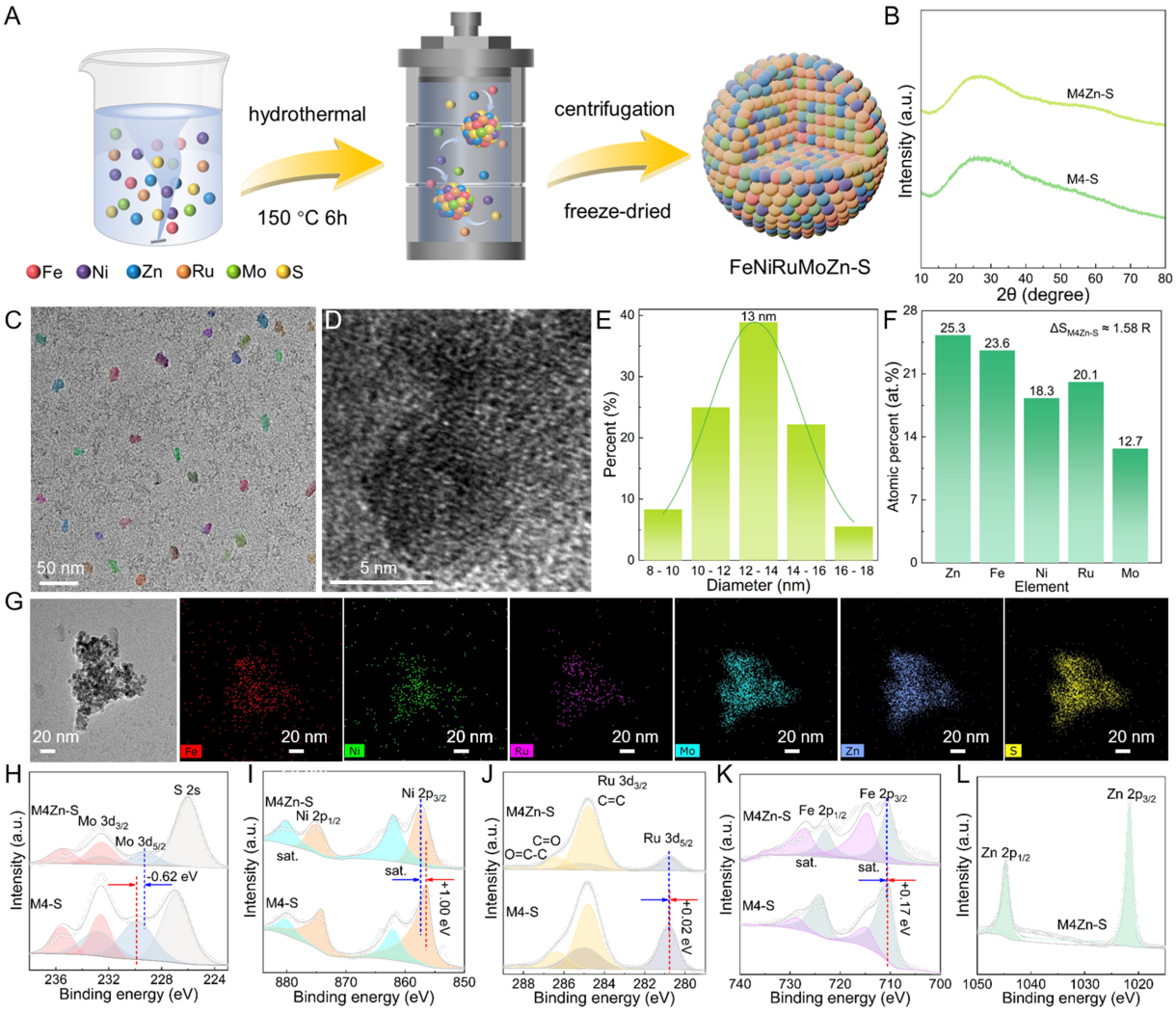

Figure 1. Synthesis and basic characterization of M4Zn-S and M4-S. (A) Hydrothermal synthesis schematic of M4Zn-S and M4-S; (B) XRD patterns of M4Zn-S and M4-S; (C) TEM images, (D) high-resolution TEM images, (E) particle size distribution, (F) elemental content analysis via ICP, and (G) TEM elemental mapping of M4Zn-S; XPS spectra including (H) Mo 3d, (I) Ni 2p, (J) Ru 3d and C 1s, and (K) Fe 2p for M4Zn-S and M4-S, as well as (L) Zn 2p for M4Zn-S. XRD: X-ray diffraction; TEM: transmission electron microscopy; ICP: inductively coupled plasma; XPS: X-ray photoelectron spectroscopy.

the same process without adding Zn, and lacks sufficient compositional complexity to access this entropic stabilization regime. Structural and morphological characterization reveals profound differences rooted in this entropy-driven design. The X-ray diffraction (XRD) patterns [Figure 1B] of both samples display broad diffraction peaks, confirming the limited long-range order typical of nanoscale sulfides. Notably, M4Zn-S exhibits slightly sharper reflections compared to M4-S, suggesting enhanced structural coherence. This is further supported by nitrogen physisorption analysis [Supplementary Figure 1], which shows that M4Zn-S possesses a higher Brunauer-Emmett-Teller (BET) surface area (17.68 $m^2 g^{-1}$) than M4-S (12.99 $m^2 g^{-1}$). These structural differences were visualized by transmission electron microscopy (TEM). As depicted in Figure 1C and D, M4Zn-S exhibits uniformly dispersed nanoparticles with clear interparticle gaps. The corresponding particle size distribution of M4Zn-S ranges from 8 to 18 nm [Figure 1E]. By contrast, M4-S tends to assemble into large interconnected aggregates, resembling merged droplets [Supplementary Figure 2].

The stark morphological contrast between M4-S and M4Zn-S can be attributed to an entropy-mediated synthesis mechanism. In the quaternary M4-S system, low configurational entropy permits rapid atomic diffusion at elevated temperatures, enabling classical Ostwald ripening. Here, smaller crystallites dissolve and

redeposit onto larger ones to minimize surface energy, ultimately yielding coarse, fused aggregates with a low surface area. In M4Zn-S, the introduction of a fifth principal element dramatically increases the configurational entropy. The actual content of each constituent element within M4Zn-S and M4-S was accurately analyzed via inductively coupled plasma (ICP) testing [Figure 1F and Supplementary Figure 3]. To quantitatively evaluate the entropic stabilization, the configurational entropy (ΔS_{config}) was estimated using the ideal solid-solution models. The calculation follows the standard formula $\Delta S_{config} = -R\Sigma(x_i \ln x_i)$, where R is the universal gas constant and x_i is the molar fraction of the metal element determined by ICP analysis[35]. Based on this formula, the quaternary M4-S yielded $\Delta S_{config} \approx 1.37R$, whereas the quinary M4Zn-S yielded a significantly higher value of ~1.58R, confirming that the latter system falls into the high-entropy regime (typically defined as $\Delta S_{config} \geq 1.5R$)[36]. Consequently, the increased configurational entropy prevents particle coarsening during hydrothermal treatment, preserving fine nuclei and yielding a high-surface-area nanostructure. The resulting morphology, combined with the entropy-tuned electronic structure, provides numerous accessible active sites and favorable charge transfer pathways, establishing a robust structural foundation for efficient electrocatalysis. Elemental mapping confirms the homogeneous distribution of all five metals (Fe, Ni, Mo, Ru, Zn) and sulfur throughout the M4Zn-S matrix, supporting the formation of a compositionally uniform solid solution [Figure 1G and Supplementary Figure 4].

X-ray photoelectron spectroscopy (XPS) was next performed to elucidate the surface electronic structure and chemical states. The survey spectrum verifies the successful incorporation of Zn, Mo, Ni, Ru, and Fe in the M4Zn-S sample [Supplementary Figure 5]. High-resolution scans [Figure 1H-L] reveal distinct signals for all constituent elements. Compared to the quaternary M4-S, the core-level peaks in M4Zn-S exhibit noticeable binding energy shifts. Specifically, the Mo $3d_{5/2}$ sulfide shifts to lower binding energy by 0.62 eV, while the Ni $2p_{3/2}$ oxide peak shifts to a higher binding energy by 1.00 eV. These features correspond to the formation of low-valence Mo and high-valence Ni species[37-40]. By contrast, the Fe $2p_{3/2}$ oxide and Ru $3d_{5/2}$ oxide peaks show minimal changes, with only slight positive shifts of 0.17 and 0.02 eV, respectively, suggesting that their electronic states remain relatively unaffected. Meanwhile, the Zn 2p spectrum confirms the presence of Zn^{2+} species in M4Zn-S. Collectively, these shifts suggest a strong electronic modulation effect induced by the high-entropy environment, in which the distinct electronegativities of the five principal elements alter the local electron density. Such electronic structure regulation is expected to optimize the adsorption energetics of reaction intermediates.

The electrocatalytic OER performance of M4Zn-S and M4-S was comprehensively evaluated in 1.0 M KOH. As shown in the linear sweep voltammetry (LSV) curves, M4Zn-S exhibits significantly higher OER activity compared to M4-S [Figure 2A]. Kinetic analysis via Tafel plots [Figure 2B] reveals that M4Zn-S exhibits a lower Tafel slope (47.6 mV dec^{-1}) compared to M4-S (59.9 mV dec^{-1}), indicating faster reaction kinetics. This suggests that the introduction of Zn boosts the intrinsic activity of metal sites and accelerates OER kinetics. Specifically, M4Zn-S requires an overpotential of only 207 mV to deliver a current density of 10 mA cm^{-2} (η_{10}), which is lower than that of M4-S (266 mV) and RuO_2 (284 mV). Even at a high current density of 100 mA cm^{-2} (η_{100}), M4Zn-S maintains a low overpotential of 262 mV, significantly outperforming M4-S (339 mV) and RuO_2 (631 mV) [Figure 2C].

Electrochemical impedance spectroscopy (EIS) was employed to investigate interfacial charge transfer dynamics. The Nyquist plots [Figure 2D] recorded at 1.50 V *vs.* RHE show a significantly smaller semicircle diameter for M4Zn-S, corresponding to a lower charge-transfer resistance (R_{ct} = 52.4 Ω) compared to M4-S (63.0 Ω; Supplementary Table 1). This reduced R_{ct} indicates improved electron transport across the electrode/electrolyte interface, facilitating the multistep OER process. Furthermore, the double-layer capacitance (C_{dl}) was determined from cyclic voltammetry (CV) measurements at multiple scan rates [Supplementary Figure 6]. The C_{dl} values of M4Zn-S and M4-S were systematically evaluated to

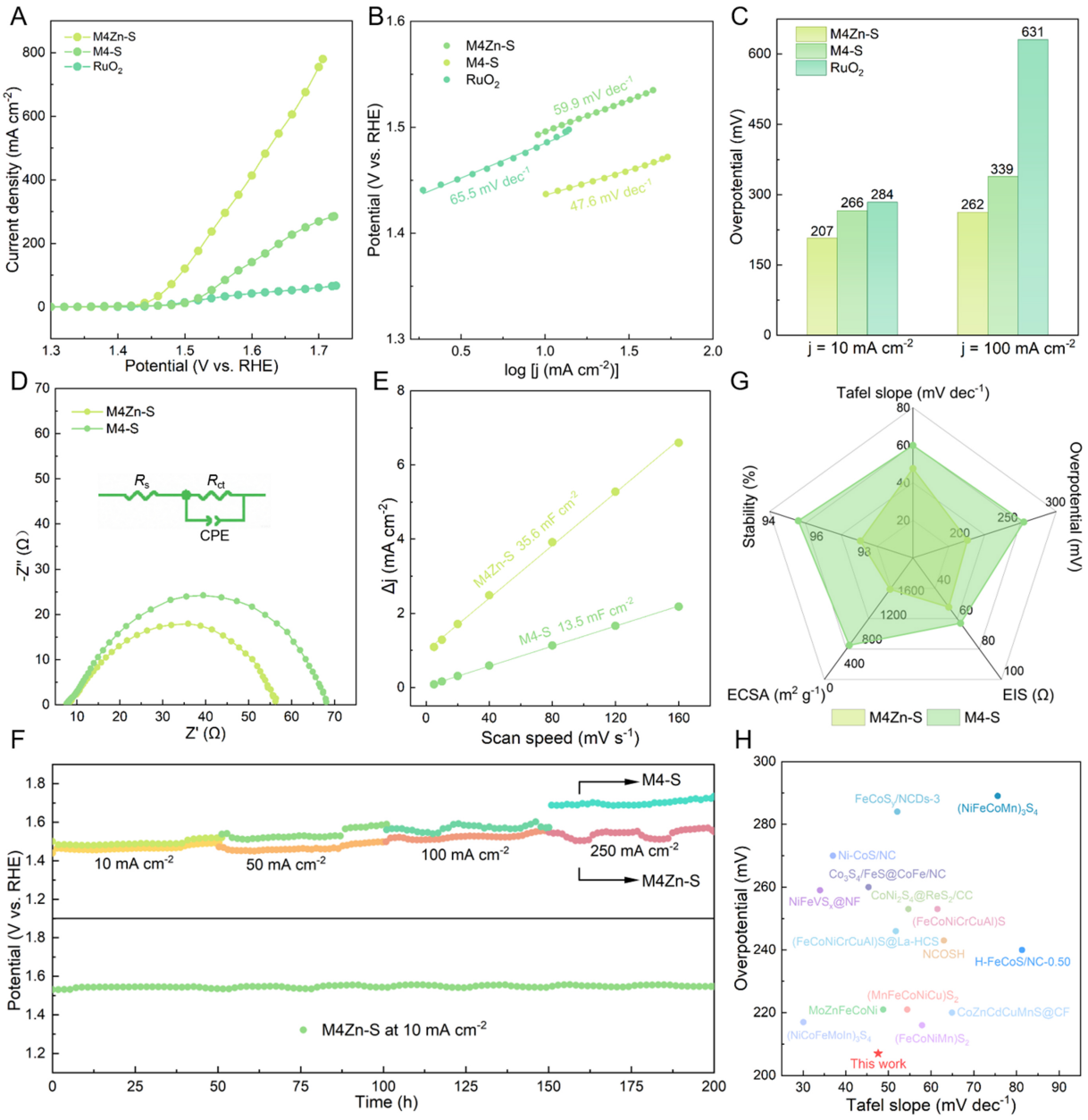

Figure 2. Electrocatalytic performance of M4Zn-S and M4-S. (A) LSV curves, (B) Tafel plots, (C) overpotentials at 10 and 100 mA cm^{-2}, (D) Nyquist plots (inset shows the fitted equivalent circuit), (E) C_{dl} values derived from multiscan-rate CV measurements, (F) long-term stability tests, and (G) performance radar chart of M4Zn-S and M4-S; (H) Comparison of Tafel slopes and overpotential with reported catalysts. LSV: Linear sweep voltammetry; CV: cyclic voltammetry.

quantitatively reflect their electrochemical active surface areas (ECSAs), a key parameter that directly correlates with the number of accessible active sites for electrochemical reactions [Figure 2E]. Remarkably, M4Zn-S exhibits a much higher C_{dl} value of 35.6 mF cm^{-2}, which is approximately 2.64 times that of M4-S (13.5 mF cm^{-2}). This significant difference in C_{dl} directly manifests the distinct ECSA characteristics between the two samples: the calculated ECSA of M4Zn-S reaches 1482.5 m^2 g^{-1}, while M4-S reaches only 562.5 m^2 g^{-1}. The nearly threefold increase in ECSA for M4Zn-S compared to M4-S can be attributed to the introduction of Zn species, which may induce structural optimization that facilitates electrolyte penetration and enlarges the interfacial contact area between the electrode and electrolyte. Such a substantial expansion of ECSA not only provides more active sites for OER but also accelerates mass transfer and charge transfer kinetics, providing a basis for the superior electrochemical performance of M4Zn-S.

The operational stability was further assessed via chronopotentiometric tests [Figure 2F]. M4Zn-S maintains stable potentials with negligible drift over extended operation at current densities ranging from 10 to 250 mA cm^{-2}. By contrast, M4-S exhibits a continuous potential increase under identical conditions. Specifically, during a 200 h test at 10 mA cm^{-2}, M4Zn-S retains a steady potential around 1.55 V *vs.* RHE. XPS analysis conducted after OER durability testing [Supplementary Figure 7] reveals the underlying stability mechanisms. M4-S shows pronounced sulfate (SO_4^{2-}) formation in the Mo 3d region [Supplementary Figure 7A], indicating irreversible structural degradation. Conversely, M4Zn-S demonstrates reversible electronic behavior. The binding energy of Mo $3d_{5/2}$ decreases [Figure 1H], while those of Ni $2p_{3/2}$ and Fe $2p_{3/2}$ initially increase [Figure 1I and K]. During operation, the binding energy of Mo $3d_{5/2}$ increases [Supplementary Figure 7A], accompanied by a reduction in the binding energies of Ni $2p_{3/2}$ and Fe $2p_{3/2}$ [Supplementary Figure 7B and C]. This dynamic redox process without sulfate formation confirms that zinc incorporation stabilizes the catalyst structure through reversible surface transformations rather than irreversible decomposition. The radar chart summarizes the overall performance comparison. M4Zn-S exhibits superior overall OER performance compared to M4-S across five key metrics: overpotential (η), Tafel slope, stability, ECSA, and R_{ct} [Figure 2G]. Collectively, these results demonstrate that the entropy-engineered M4Zn-S achieves a superior balance of high intrinsic activity and robust structural stability, making it a promising candidate for industrial-scale water splitting. Furthermore, M4Zn-S surpasses the performance of recently reported state-of-the-art OER electrocatalysts, distinguished by its exceptionally low overpotential and small Tafel slope [Figure 2H and Supplementary Table 2].

In situ spectroscopic characterization was next performed to gain molecular-level insight into the OER mechanism. Figure 3A schematically illustrates the conventional adsorbate evolution mechanism (AEM), LOM, and OPM. While AEM is often limited by scaling relations, LOM involves direct lattice oxygen participation, offering a pathway to bypass these thermodynamic constraints. In addition, AEM and LOM mechanisms are widely recognized, while OPM is generally considered another plausible reaction pathway. The key feature of OPM is that the adjacent surface-adsorbed oxygen species can directly couple to form the O-O bond without requiring the *OOH intermediate, and it typically does not involve the direct participation of lattice oxygen[41].

In situ infrared (IR) spectroscopy was employed to identify the reaction pathway (the IR setup and measurement procedure are detailed in the Supplementary Materials). As shown in Figure 3B, a distinct peak emerges at 949 cm^{-1}, which is assigned to M-*O. The peak at 1,103 cm^{-1} corresponds to M-O-O-M. Additionally, a weak absorption band centered at 1,290 cm^{-1} is detected and assigned to *OH. The prominent M-*O peak indicates sufficient accumulation of *O reaction intermediates, which promotes the subsequent generation of M-O-O-M configurations and consequently facilitates the OPM mechanism[42,43]. This spectral evolution strongly indicates that the OER process on M4Zn-S follows OPM, in which adjacent adsorbed oxygen species directly couple to form the O-O bond, and no direct participation of lattice oxygen is involved during the reaction. By contrast, the M-*O peak of M4-S is weak [Figure 3C]. Furthermore, no *OH signal can be detected around 1,290 cm^{-1} due to the high activation energy of the hydroxide ions. Elevated potentials trigger the sequential transformation of M-*OH to M-*O and subsequently M-*O-O. Such evolution proceeds via intramolecular coupling between adsorbed hydroxyl species and lattice oxygen to form O-O bonds. The distinct M-*O-O signal at 1,106 cm^{-1} indicates that the OER process on M4-S exhibits features characteristic of LOM.

The *in situ* IR results show that the OER pathways of M_4Zn-S and M_4-S differ mainly in the mode of O-O bond formation and the involvement of lattice oxygen. For M_4Zn-S, the pronounced O-O signal indicates that adjacent surface-adsorbed oxygen species directly couple to form the O-O bond, which is characteristic of the OPM. Therefore, M4Zn-S follows an adsorbed-oxygen coupling route, whereas M_4-S relies more

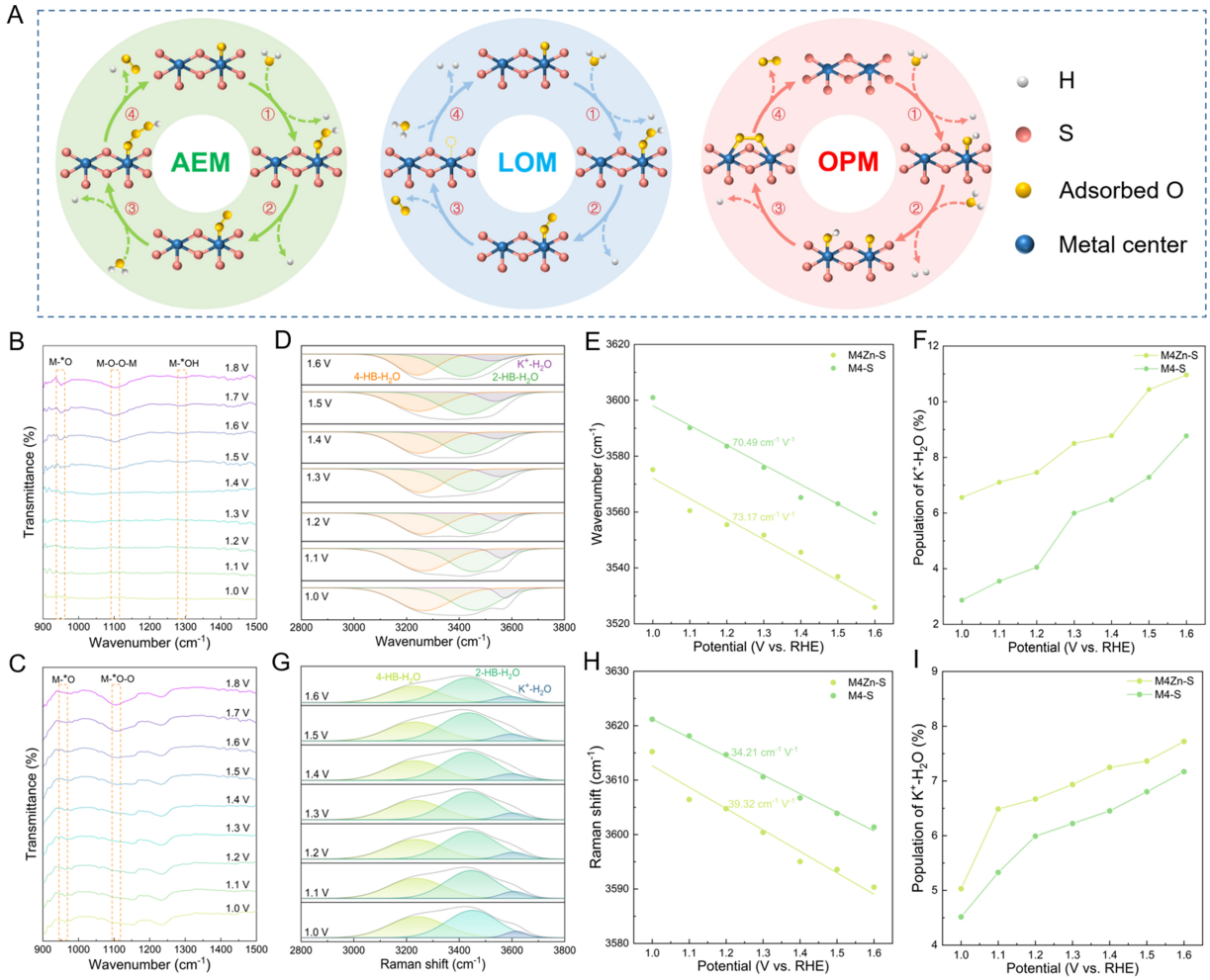

Figure 3. Catalytic mechanism analysis of M4Zn-S and M4-S. (A) Schematic of the AEM, LOM, and OPM; (B and C) *In situ* IR spectra (900-1,500 cm^{-1}) of M4Zn-S and M4-S. Analysis of the interfacial water structure via (D-F) *in situ* IR and (G-I) Raman spectroscopy: (D and G) spectral deconvolution, (E and H) stark tuning slopes of the K^+-H_2O band, and (F and I) relative abundance of K^+-H_2O. AEM: Adsorbate evolution mechanism; LOM: lattice oxygen-mediated mechanism; OPM: oxide pathway mechanism; IR: infrared.

strongly on lattice oxygen participation, which can accelerate structural reconstruction and stability loss during OER.

To understand how the interfacial environment facilitates this process, we investigated the structure of interfacial water molecules and their interaction with alkali cations. As shown in Figure 3D, the *in situ* IR spectra of M4Zn-S reveal distinct vibrational features associated with the K^+-H_2O coordination shell in the O-H stretching region (approximately 3,000-3,700 cm^{-1}), indicating the presence of a well-defined cation-hydration layer at the catalyst surface. The stark tuning slope of the K^+-H_2O vibrational band [Figure 3E] reflects the sensitivity of the interfacial water structure to the applied potential. Notably, this slope is significantly steeper for M4Zn-S in the IR measurements compared to M4-S, and the relative population of K^+-H_2O is markedly higher for M4Zn-S [Figure 3F]. Similarly, the Raman spectra [Figure 3G] confirm these trends, showing a steeper stark tuning slope [Figure 3H] and a higher relative population of K^+-H_2O [Figure 3I] for M4Zn-S, implying a greater accumulation of hydrated K^+ ions near the active surface.

This engineered interfacial microenvironment is critical for the enhanced kinetics. In alkaline media, the accumulated K^+ ions are conducive to breaking the hydrogen-bond network, and they are beneficial for the transfer and adsorption of OH at active sites[44]. The rapid OER kinetics of M4Zn-S foster a favorable OPM

via interfacial water modulation and may account for a lower Tafel slope (47.6 mV dec^{-1}) and low overpotential (207 mV at 10 mA cm^{-2}). Thus, the high-entropy design of M4Zn-S not only tunes the bulk electronic structure but also actively optimizes the local reaction environment, a dual-function advantage that is rarely achieved by conventional catalysts.

We next performed DFT calculations to further elucidate the catalytic mechanism. Based on the experimental characterizations, a slab model based on MoS_2 was constructed, with the metallic M4Zn-S and M4-S systems substituting the Mo sites [Figure 4A]. The projected density of states (PDOS) results demonstrate high-entropy modulation of the electronic structure. In M4Zn-S, Zn incorporation rearranges the d-electron distribution of the Fe and Ni active sites [Figure 4B and C]. The d-band center of Ni in M4Zn-S shifts upward from -3.085 to -2.602 eV, increasing the adsorption affinity toward OER intermediates. Meanwhile, the Fe d-band center shifts moderately downward from -2.047 to -2.440 eV, mitigating the excessive adsorption of oxygen-containing intermediates. The synergistic modulation balances the intermediate adsorption strength, matching the optimal OER pathway and lowering reaction barriers[45]. Improper d-band positions in M4-S induce unfavorable adsorption behaviors and sluggish catalytic kinetics. Bader charge analysis also confirms that high-entropy engineering induces charge redistribution in M4Zn-S, enhancing electron donation from metal sites, tuning the d-band centers, and balancing intermediate adsorption to accelerate OER kinetics[46] [Figure 4D].

We compared the differential charge-density distribution of Fe and Ni sites in M4Zn-S and M4-S to further clarify the modulation of the reaction pathway and electronic structure resulting from Zn incorporation [Figure 4E and F]. In M4Zn-S, the suppressed electron depletion around the Fe sites reduces the excessive electron transfer to O intermediates, matching the downshifted d-band center and alleviating the structural instability caused by strong Fe-lattice oxygen interactions. Meanwhile, enhanced electron accumulation and polarization around the Ni sites indicate improved OH adsorption activation following d-band center upshifting[47]. Critically, efficient electronic coupling between Fe and Ni in M4Zn-S produces a continuous charge distribution that facilitates the direct coupling of adjacent O species, consistent with the OPM mechanism. By contrast, as M4-S exhibits overly strong Fe interactions and insufficient Ni activation, it cannot establish such synergy and instead favors the LOM pathway. These results directly indicate Zn-induced dual-site electronic optimization, evidencing the superior OER performance of M4Zn-S.

The free-energy diagrams and electronic structure analyses demonstrate that M4Zn-S favors OPM for OER, differing from the LOM observed in M4-S [Figure 4G]. Unlike the conventional AEM, the OPM pathway in M4Zn-S proceeds via the direct O-O coupling of two adjacent adsorbed O species, eliminating the typical *OOH formation step. The d-band center and PDOS results reveal that Zn incorporation tunes the dual-site electronic structure. In this system, the upshifted Ni d-band center enhances OH activation, while the moderately downshifted Fe d-band center optimizes O intermediate adsorption, collectively enabling favorable O-O coupling. The higher density of states (DOS) observed near the Fermi level further facilitates efficient electronic coupling between sites, promoting *O-O formation and reducing the Gibbs free-energy change of PDS from 2.460 to 1.761 eV. This OPM pathway circumvents the scaling relation constraints of AEM and avoids the structural degradation induced by lattice oxygen participation in LOM, enabling the simultaneous high activity and stability of M4Zn-S.

The DFT results reveal a clear synergistic modulation of the dual active sites induced by Zn incorporation. The upward shift of the Ni d-band center strengthens the adsorption and activation of hydroxyl species, which is critical for the initial step of the OER. Meanwhile, the moderate downward shift of the Fe d-band center alleviates excessive adsorption of oxygen-containing intermediates. This balanced electronic modulation, wherein Ni promotes activation and Fe prevents overbinding, enables synergistic coupling

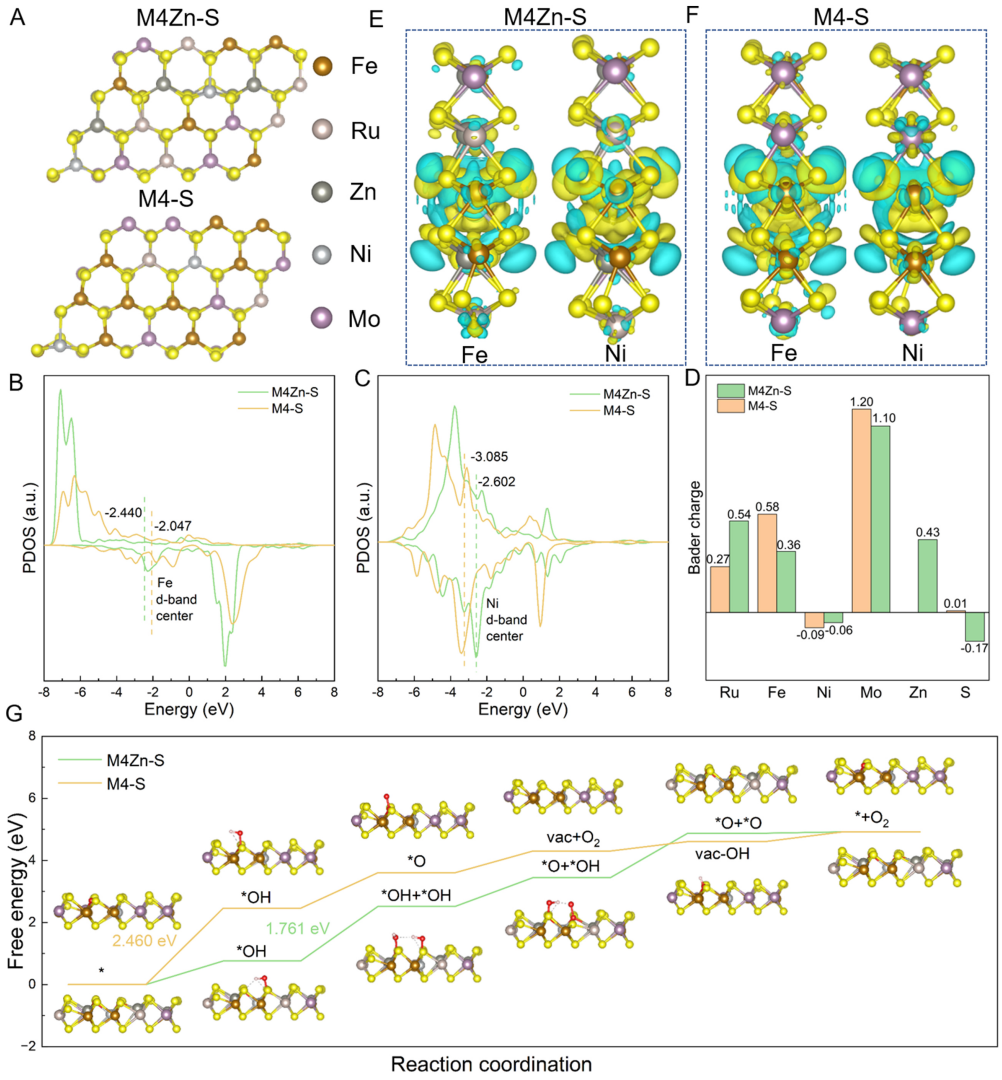

Figure 4. DFT-based analysis of the catalytic mechanism. (A) Top views of M4Zn-S and M4-S; PDOS of (B) Fe and (C) Ni for M4Zn-S and M4-S; (D) Bader charge analysis of different elements for M4Zn-S and M4-S; Bader charge map of Fe and Ni in (E) M4Zn-S and (F) M4-S; (G) Free-energy diagrams of OPM for M4Zn-S and LOM for M4-S. PDOS: Projected density of states; DFT: density functional theory; OPM: oxide pathway mechanism; LOM: attice oxygen-mediated mechanism.

between adjacent metal sites. Consequently, the Gibbs free-energy change of PDS is significantly reduced from 2.460 to 1.761 eV, while the direct O-O coupling pathway is kinetically favored without invoking lattice oxygen participation.

An AEMWE was constructed to evaluate the practical application potential of the synthesized catalysts. The device configuration [Figure 5A] employs Pt/C as the hydrogen evolution reaction (HER) cathode and the as-prepared M4Zn-S (or commercial RuO_2 for comparison) as the OER anode, separated by an anion exchange membrane. The overall water-splitting performance was first evaluated by recording polarization curves at room temperature (RT, ~25 °C). The electrolyzer integrated with the Pt/C||M4Zn-S couple exhibits remarkable electrocatalytic activity, significantly outperforming the Pt/C||RuO_2 reference cell [Figure 5B]. Specifically, the M4Zn-S-based electrolyzer delivers a current density of 1 A cm^{-2} at a low cell voltage of 1.90 V. By contrast, the RuO_2-based electrolyzer requires a higher voltage to drive the same current density, highlighting the superior kinetic activity of the M4Zn-S catalyst in a practical device environment.

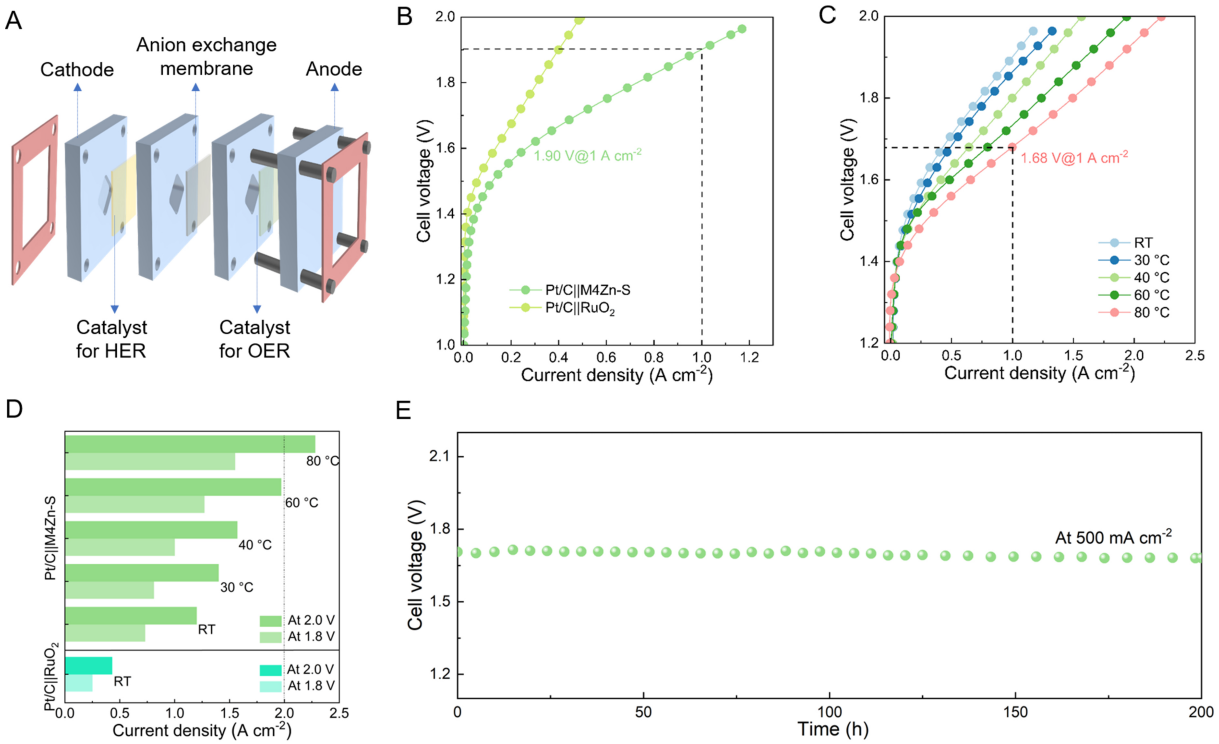

Figure 5. Evaluation of the overall electrolysis water performance of Pt/C||M4Zn-S based on AEMWE. (A) Schematic of the electrolyzer configuration; (B) Polarization curves of Pt/C||M4Zn-S and Pt/C||RuO_2; (C) Temperature-dependent polarization curves of Pt/C||M4Zn-S; (D) Corresponding current densities at 1.8 and 2.0 V for Pt/C||M4Zn-S from RT to 80 °C and Pt/C||RuO_2 at RT; (E) Chronopotentiometric stability test conducted at 500 mA cm^{-2}. AEMWE: Anion exchange membrane water electrolyzer; RT: room temperature.

The temperature-dependent performance of the Pt/C||M4Zn-S electrolyzer was systematically investigated considering the actual industrial temperature used for water electrolysis [Figure 5C]. Elevated temperatures generally improve reaction kinetics and ionic conductivity, and the investigated system delivers a current density of 1 A cm^{-2} at 1.68 V. The polarization curves reveal a strong positive correlation between the operating temperature and cell performance. As the temperature increases from RT to 80 °C, the cell voltage required to achieve a specific current density gradually decreases. This trend is quantitatively summarized in Figure 5D, which compares the current densities at constant voltages of 1.8 and 2.0 V. At 80 °C, the electrolyzer achieves a high current density of approximately 2.3 A cm^{-2} at 2.0 V, whereas at RT, the current density is less than 1.2 A cm^{-2}. This significant enhancement is attributed to the accelerated reaction kinetics and reduced ohmic resistance achieved at higher temperatures. Finally, the long-term durability of the Pt/C||M4Zn-S electrolyzer was assessed via chronopotentiometric testing at a constant current density of 500 mA cm^{-2}. The cell voltage maintained a stable plateau around 1.72 V during 200 h of continuous operation, with no observable degradation or fluctuation [Figure 5E]. TEM elemental mapping, XRD, and XPS analyses were conducted to verify that the catalyst structure and composition were preserved after AEMWE operation. TEM elemental mapping indicates that all metal elements remain uniformly distributed on the catalyst surface without elemental segregation or loss, further verifying the structural and compositional integrity of M4Zn-S [Supplementary Figure 8]. The XRD characteristic diffraction peaks of M4Zn-S [Supplementary Figure 9A] and M4-S [Supplementary Figure 9B] are consistent with those of the fresh sample after electrolysis. No new miscellaneous peaks or peak shifts are observed, indicating that no phase transition or crystal structure degradation occurred under harsh OER conditions. In addition, there was no significant shift in the peak shape and binding energy between the main and satellite peaks of Fe 2p and Ni 2p, indicating that the valence states of Fe and Ni coordination remained stable, and no severe

oxidative reconstruction occurred. The Ru 3p peak positions barely shifted before and after AEMWE operation, whereas only minor intensity variations are observed for the Mo 3d characteristic peaks. Both the binding energies and intensities of Zn 2p remain nearly unaltered. By contrast, the overall intensity of the S 2p spectra moderately declines post-reaction, indicating mild leaching of sulfur species. Such slight sulfur dissolution facilitates the S-O exchange pathway and thus favors the onset of the OER process [Supplementary Figure 10]. In addition, ICP analysis verified the sulfur anti-oxidation and anti-leaching effect induced by Zn doping, and it further confirmed the structural retention of Zn active sites during long-term AEMWE. The ICP results [Supplementary Figure 11] show that only a trace amount of sulfur is detected in the post-operation electrolyte, and the sulfur leaching is only 0.12 ppm of M4Zn-S after 100 h of continuous AEMWE operation. By contrast, the M4-S counterpart exhibits greater sulfur leaching (0.46 ppm). Moreover, the Zn retention rate remains at 100% after 100 h of long-term AEMWE operation, verifying negligible Zn leaching during the harsh OER process. In addition, the amount of Fe, Ru, and Mo dissolved in the electrolyte after cycling for M4Zn-S is lower than that for M4-S. This quantitative difference directly confirms that the introduced Zn component effectively suppresses sulfur dissolution [Supplementary Figure 11].

From an industrial application perspective, the M4Zn-S anode offers compelling advantages over conventional RuO_2-based anodes for AEMWEs. First, in terms of material cost, M4Zn-S is composed of earth-abundant transition metals (Fe, Ni, Mo, Zn) and Ru, substantially reducing the overall catalyst cost and mitigating supply chain concerns associated with precious-metal dependence. Second, unlike RuO_2-based anodes that undergo obvious performance fading in alkaline electrolytes, M_4Zn-S follows the OPM without lattice oxygen involvement and thus maintains structural stability during long-term electrolysis. This mechanistic distinction is directly reflected in the device-level durability, as the Pt/C||M_4Zn-S electrolyzer retains a steady ~1.72 V voltage plateau at 500 mA cm^{-2} for 200 h with no degradation, outperforming many state-of-the-art nonprecious-metal anodes and rivaling or surpassing RuO_2-based devices in both activity and stability [Supplementary Table 2]. Collectively, these results underscore that the combination of a predominantly earth-abundant composition, OPM-enabled structural durability, and excellent device-level performance positions M4Zn-S as a promising, cost-effective, and durable alternative to precious-metal-based anodes for practical AEMWE applications.

The incorporation of Zn into the FeNiMoRu-S system fundamentally transforms its physicochemical properties through a hierarchically coupled stabilization mechanism, operating across multiple length scales, which is detailed as follows. (1) Nanoscale structural control via high-entropy stabilization. As the fifth principal element, Zn elevates the system into the high-entropy regime. The resulting high configurational entropy thermodynamically stabilizes the solid-solution phase and kinetically suppresses Ostwald ripening through the "sluggish diffusion effect", yielding well-dispersed nanoparticles with a significantly higher BET surface area (17.68 *vs.* 12.99 m^2 g^{-1}) and enhanced crystallinity; (2) Interfacial water structure engineering enabled by optimized morphology. The resulting high-surface-area nanostructure, combined with a Zn-modulated surface chemistry, promotes the accumulation of a dense K^+-H_2O hydration layer at the electrode/electrolyte interface. This engineered interfacial environment polarizes adsorbed water molecules, facilitating O-H bond cleavage and stabilizing key OER intermediates, thereby directly enabling the observed superior kinetics (Tafel slope: 47.6 mV dec^{-1}) and low overpotential (207 mV at 10 mA cm^{-2} and 262 mV at 100 mA cm^{-2}); (3) Atomic-level chemical stabilization underpinning long-term durability. Critically, Zn incorporation stabilizes the sulfur anion sublattice against irreversible oxidative corrosion. Post-OER XPS analysis confirms that while M4-S suffers severe sulfate (SO_4^{2-}) formation, M4Zn-S retains its intact sulfide framework. This atomic-scale integrity is the foundation for reversible redox cycling of all active cations, in stark contrast to the irreversible degradation (e.g., anomalous Ni oxidation) observed in M4-S. Therefore, Zn is not a passive dopant but an active component, as it first establishes a robust nanostructure that, in turn,

enables a reactive interfacial microenvironment, and this system includes the atomic-level protection of the anionic lattice. These multiscale synergistic effects improve the morphological structure, interfacial engineering, and chemical stability of this system, rendering M4Zn-S an efficient and robust OER electrocatalyst.

CONCLUSIONS

This work demonstrates that the enhanced OER performance of FeNiMoRuZn sulfide directly results from Zn-enabled multiscale stabilization via synergistic effects spanning the atomic, nanoscale, and interfacial domains. The introduction of Zn as a fifth principal element not only elevates the system into the high-entropy regime to kinetically suppress particle aggregation during synthesis but also fundamentally alters the resilience of the catalyst under operational conditions. In particular, the preserved sulfur lattice prevents irreversible phase transformation, the high-surface-area nanostructure maximizes active site exposure, and the engineered electrode/electrolyte interface accelerates water activation kinetics. Together, these interconnected effects enable the sustained, reversible redox cycling of all active metal centers, which is unattainable in the Zn-free analog due to sulfur corrosion and structural collapse. The success of this approach underscores a broader design principle indicating that the strategic selection of a single component can simultaneously govern the structural coherence, interfacial reactivity, and anion stability of complex multi-principal-element electrocatalysts. While the current study demonstrated this principle for the alkaline OER, this multiscale stabilization paradigm may be extended to other anion-based energy conversion systems in which the maintenance of lattice integrity under harsh electrochemical conditions is challenging.

DECLARATIONS

Authors' contributions

Methodology, formal analysis, and writing of the manuscript: Gao, S.
Data acquisition: Guan, J.
Data analysis and technical support: Chen, H.
Electrochemical performance measurements: Mao, F.
Analysis and interpretation of the results: Lei, J.; Guo, D.
Writing - review and editing, Visualization: Gao, Y.
Supervision, funding acquisition, writing - review and editing: Li, Y.; Shao, G.

Availability of data and materials

The raw data supporting the findings of this study are available within this Article and its Supplementary Materials. Further data are available from the corresponding authors upon request.

AI and AI-assisted tools statement

During the preparation of this manuscript, the AI tool Qwen image generation tool (version Qwen3.7, released 2026-05-20) was used solely to generate the lightning elements in the Graphical Abstract. The tool did not influence the study design, data collection, analysis, interpretation, or the scientific content of the work. All authors take full responsibility for the accuracy, integrity, and final content of the manuscript.

Financial support and sponsorship

This work was supported by the National Natural Science Foundation of China under Grant No. 22205209, the China Postdoctoral Science Foundation under Grant No. 2024T170837, Henan Province's Central Plains Talent Program (Cultivation Series)-Young Top Talents of Central Plains, the Natural Science Foundation of Henan under Grant Nos. 242301420039 and 262300422440, the Startup Research Fund of Henan Academy of Sciences under Grant No. 20261842003, the Nanhu Scholars Program for Young Scholars of XYNU and the Analysis Testing Center of Xinyang Normal University.

Conflicts of interest

All authors declared that there are no conflicts of interest.

Ethical approval and consent to participate

Not applicable.

Consent for publication

Not applicable.

Supplementary Materials

Supplementary Materials

REFERENCES

1. Cao, Y.; Gao, L.; Liu, Y.; Lin, Z. Harnessing magnetic, photo, and thermal fields and their synergistic interactions for enhanced electrocatalytic oxygen evolution reaction. *Chem. Soc. Rev.* **2026**, *55*, 1371-410. DOI
2. Yu, A.; Wu, T.; Ren, X.; Xu, Z. J. Spin-promotion effect to oxygen evolution reaction. *Acc. Chem. Res.* **2025**, *58*, 3273-80. DOI PubMed PMC
3. Liu, S.; Ban, Y.; Liu, Y.; et al. Engineering geometric active sites in cobalt spinel oxides for energy and environmental catalysis. *Rare. Metals.* **2026**, *45*, e70207. DOI
4. Shi, L.; Zhang, W.; Li, J.; et al. Recent development of non-iridium-based electrocatalysts for acidic oxygen evolution reaction. *Carbon. Neutralization.* **2024**, *3*, 1101-30. DOI
5. Mu, J.; Liu, S.; Yu, C.; et al. Intensified accumulation of OH^- and improved electron transfer by reactive chlorine-resistant layer achieve high-durability seawater electrolysis. *Adv. Mater.* **2026**, *38*, e20960. DOI
6. Biswal, S.; Kumari, A.; Mishra, B.; Ghosh, D.; Tripathi, B. P. Ferromagnetic synergy in a ruthenium single-atom catalyst on $NiCo_2S_4$ for magnetically enhanced water splitting. *ACS. Catal.* **2026**, *16*, 7246-65. DOI
7. Zhang, N.; Hu, Y.; Zhang, Z.; et al. Crystallinity-dependent structural evolution of CoS_2 catalysts for enhanced oxygen evolution reaction. *Nat. Commun.* **2025**, *16*, 9306. DOI PubMed PMC
8. Wang, R.; Deng, X.; Hu, B.; et al. Advances in transition metal sulfides: synthesis, properties, and modification strategies for electrocatalysis and energy conversion applications. *Coord. Chem. Rev.* **2026**, *559*, 217797. DOI
9. Zhu, D.; Zan, L.; Tu, Y.; et al. Disclosing the intrinsic electrocatalytic activity of transition-metal sulfides for enhanced water oxidation. *Sci. China. Chem.* **2025**, *68*, 4441-9. DOI
10. Han, Q.; Luo, Y.; Li, J.; et al. Efficient NiFe-based oxygen evolution electrocatalysts and origin of their distinct activity. *Appl. Catal. B. Environ.* **2022**, *304*, 120937. DOI
11. Xiao, Y.; Zhang, S.; Shen, Y.; et al. Optimizing the intermediates adsorbability and revealing the dynamic reconstruction of $Co_6Fe_3S_8$ solid solution for bifunctional water splitting. *J. Colloid. Interface. Sci.* **2024**, *664*, 329-37. DOI
12. Chen, M.; Li, W.; Lu, Y.; et al. In situ fabrication of low-crystallinity $(Ni,Fe)_xS_y$ nanosheet arrays via room-temperature corrosion engineering toward efficient oxygen evolution. *Appl. Catal. B. Environ. Energy.* **2024**, *358*, 124415. DOI
13. Sun, Y.; Sun, Y.; Zhang, Y.; Yanagida, T.; Ho, J. C.; Yip, S. Iron-cobalt co-doped nickel sulfides: a robust electrocatalyst for high-current-density seawater splitting. *Adv. Funct. Mater.* **2026**, *36*, e17978. DOI
14. Cai, H.; He, S.; Yang, H.; et al. Highly exposed ultra-small high-entropy sulfides with d-p orbital hybridization for efficient oxygen evolution. *Adv. Mater.* **2025**, *37*, e2508610. DOI
15. Gao, T.; Wang, W.; Zhang, Z.; et al. Dual-anion regulation engineering enhances chloridion corrosion resistance for long-lasting industrial-scale seawater splitting. *Chem. Sci.* **2025**, *16*, 15684-96. DOI PubMed PMC
16. He, C.; Pan, D.; Li, X.; et al. Fresh perspectives and insights into the challenges and opportunities in the emerging high-entropy electrocatalysts. *Coord. Chem. Rev.* **2025**, *531*, 216496. DOI
17. Xu, J.; Sun, H.; Cai, F.; et al. Single-nanoparticle collision revealing high-entropy suppression of elemental segregation in multi-element alloys during oxygen evolution reaction. *Angew. Chem. Int. Ed.* **2026**, *65*, e22707. DOI
18. Iwase, K.; Honma, I.; Tomai, T. Unveiling synergistic elemental roles in high-entropy spinel oxides for oxygen evolution electrocatalysis. *ACS. Catal.* **2026**, *16*, 7395-403. DOI
19. Dai, Y.; Tu, X.; Yue, K.; et al. Anti-dissolving high entropy phosphorus sulfide for efficient and durable seawater electrolysis. *Adv. Funct. Mater.* **2025**, *35*, 2417211. DOI

20. Wang, G.; Fan, L.; Wang, P.; Wang, J.; Qiao, F.; Wen, Z. Efficient synthesis of nano high-entropy compounds for advanced oxygen evolution reaction. *Chin. Chem. Lett.* **2025**, *36*, 110498. DOI
21. Jiang, L.; Duan, B.; Lin, S.; et al. High-entropy chalcogenides via ambient and scalable synthesis for efficient OER catalysis. *Nano. Energy.* **2026**, *148*, 111634. DOI
22. Zhang, Q.; Wang, Z.; Wang, L.; et al. Nano-hollow carbon-supported high-entropy alloy catalysts for energy-saving seawater electrolysis. *Nano. Res. Energy.* **2025**, *4*, e9120196. DOI
23. Zang, S.; Hou, Y.; Chang, J.; et al. Amorphous-crystalline heterostructures enable energy-level matching of cobalt sulfide/nickel iron layered double hydroxide for efficient oxygen evolution reaction. *J. Colloid. Interface. Sci.* **2024**, *656*, 485-94. DOI
24. Li, S.; Ma, Z.; Fu, M.; et al. Anion/cation-induced strong electronic polarization of N,Fe-CoS_2 electrocatalyst to boost efficient oxygen evolution. *J. Colloid. Interface. Sci.* **2024**, *654*, 1089-97. DOI
25. Xue, Y.; Liu, M.; Qin, Y.; et al. Ultrathin NiFeS nanosheets as highly active electrocatalysts for oxygen evolution reaction. *Chin. Chem. Lett.* **2022**, *33*, 3916-20. DOI
26. Wang, C.; Wu, Y.; Zhou, Z.; Wang, J.; Pei, S.; Liu, S. Electrodeposited amorphous nickel-iron phosphide and sulfide derived films for electrocatalytic oxygen evolution. *Int. J. Hydrogen. Energy.* **2022**, *47*, 40849-59. DOI
27. Deore, S. Oxide melt solution calorimetry of sulfides: enthalpy of formation of sphalerite, galena, greenockite, and hawleyite. *Am. Mineral.* **2006**, *91*, 400-3. DOI
28. Dengo, N.; Vittadini, A.; Natile, M. M.; Gross, S. In-depth study of ZnS nanoparticle surface properties with a combined experimental and theoretical approach. *J. Phys. Chem. C.* **2020**, *124*, 7777-89. DOI
29. Jia, X.; Chen, H.; Sun, H.; Zhu, J.; Lu, B. Promoting robust potassium storage via engineered Zn-S bond. *Adv. Energy. Mater.* **2025**, *15*, 2501487. DOI
30. Liang, W.; Chen, B.; Li, D.; et al. Understanding the structural relation and electrochemical evolution between $ZnGeP_2$ and $ZnSiP_2$ twin phosphides for advanced Li-ion batteries. *Chem. Eng. J.* **2024**, *496*, 154332. DOI
31. Brunca da Silva, A.; Arizono Dos Reis, E.; Ribeiro, C.; Helena Mascaro, L. Overcoming stability hurdles of transition metal phosphides for H_2 evolution: a review. *ChemSusChem* **2025**, *18*, e202501388. DOI PubMed PMC
32. Brad, A. J.; Faulkner, L. R. *Electrochemical methods: fundamentals and applications*, 2th ed.; John Wiley & Sons, 2001. https://eva.fcien.udelar.edu.uy/pluginfile.php/144317/mod_resource/content/3/Electrochemical%20Methods%20Bard%20Faulkner%20Cap1-4.pdf (accessed 2026-08-10).
33. Nørskov, J. K.; Rossmeisl, J.; Logadottir, A.; et al. Origin of the overpotential for oxygen reduction at a fuel-cell cathode. *J. Phys. Chem. B.* **2004**, *108*, 17886-92. DOI
34. Bligaard, T.; Nørskov, J.; Dahl, S.; Matthiesen, J.; Christensen, C.; Sehested, J. The Brønsted-Evans-Polanyi relation and the volcano curve in heterogeneous catalysis. *J. Catal.* **2004**, *224*, 206-17. DOI
35. Yeh, J.; Chen, S.; Lin, S.; et al. Nanostructured high-entropy alloys with multiple principal elements: novel alloy design concepts and outcomes. *Adv. Eng. Mater.* **2004**, *6*, 299-303. DOI
36. Wang, R.; Kang, Q.; Wang, R.; et al. Understanding the key factors in high entropy electrocatalysts for an efficient oxygen evolution reaction. *J. Energy. Chem.* **2025**, *110*, 788-822. DOI
37. Song, Z.; Min, H.; Zhu, M.; et al. Tensile strain-mediated cobalt nitrides by high-valence metal modulator enable oxygen evolution performance. *Adv. Funct. Materials.* **2026**, *36*, e23085. DOI
38. Zhang, Y.; Xia, Q.; Wang, J.; et al. Electrocatalysis-dependent dynamic surface reconstruction of redox couples for bifunctional electrocatalysts. *Appl. Catal. B. Environ. Energy.* **2025**, *376*, 125468. DOI
39. Wu, D.; Hu, L.; Liu, X.; et al. Time-resolved spectroscopy uncovers deprotonation-induced reconstruction in oxygen-evolution NiFe-based (oxy)hydroxides. *Nat. Commun.* **2025**, *16*, 726. DOI PubMed PMC
40. Wang, Z.; Feng, J.; Chen, S.; et al. High-valent nickel oxyhydroxides self-derived through a low-temperature thermochemical strategy for an efficient oxygen evolution reaction. *J. Colloid. Interface. Sci.* **2025**, *699*, 138243. DOI
41. Zhang, D.; Li, M.; Yong, X.; et al. Construction of Zn-doped RuO_2 nanowires for efficient and stable water oxidation in acidic media. *Nat. Commun.* **2023**, *14*, 2517. DOI PubMed PMC
42. Cao, X.; Qin, H.; Zhang, J.; Chen, X.; Jiao, L. Regulation of oxide pathway mechanism for sustainable acidic water oxidation. *J. Am. Chem. Soc.* **2024**, *146*, 32049-58. DOI
43. Zhang, J.; Cao, X.; Qin, H.; Ma, R.; Jiao, L. Switching to the oxide path mechanism on solid-solution Ru-O-Ti bridge architectures for efficient and stable acidic water oxidation. *CCS. Chem.* **2026**, 1-25. DOI
44. Hong, Q. L.; Xiao, X.; Ai, X.; et al. Organic interface enhanced electrocatalysis. *Chem. Soc. Rev.* **2025**, *54*, 9849-75. DOI
45. Wang, B.; Luo, Z.; Sun, H.; et al. Electronic modulation of amorphous/crystalline NiFe LDH by atomic Pt loading enabling industrial hydrogen production in alkaline water and seawater. *J. Energy. Chem.* **2025**, *107*, 427-39. DOI

46. Zhao, X.; Zheng, H.; Sun, H.; et al. Interfacial component coupling effects induce electron redistribution for enhanced hydrazine-assisted hydrogen production at ampere-level current densities. *Nano. Energy.* **2025**, *142*, 111201. DOI
47. Sun, H.; Chen, M.; Xiao, B.; et al. Interface engineering induced electron redistribution at Pt(Ns) /NiTe-Ns interfaces for promoting pH-universal and chloride-tolerant hydrogen evolution reaction. *Small* **2023**, *19*, e2303974. DOI